Numerical Simulation of Gas Tungsten Arc Welding in Different Gaseous Atmospheres†

TASHIRO Shinichi *, TANAKA Manabu ** and USHIO Masao ***

Abstract

In order to clarify the formative mechanism of penetration geometry at the anode in an arc melting process using gas tungsten arc plasma, a numerical model is useful to understand quantitative values for the balances of mass, energy and force in the melting phenomena. In the present paper, the whole region of an arc melting process, namely, tungsten cathode, arc plasma and anode is treated in a unified numerical model to take into account the close interaction between the arc plasma and the liquid anode. Calculations are made for the time dependent development of the penetration at the anode for the arc plasma in different gaseous atmosphere at a current of 150 A. The anode penetration geometry as a function of time is predicted in the arc melting process in argon and also helium.

KEY WORDS: (Numerical model), (Arc plasma), (Anode), (Melting), (Welding), (Fluid flow), (Argon), (Helium).

1. Introduction

Arc plasmas have been applied in the industrial processing of materials, for example in surface treatment, arc furnaces, the processing of minerals and in arc melting. Probably the most important application in arc melting is arc welding. For the understanding and also the control of such processes, it is important to develop a modeling capability, preferably to be able to predict properties of the total arc processing system. For example, in arc welding, one of the most important parameters is the geometry of the weld penetration, as this geometry determines the thickness and thus the strength of the weld. The principal control parameter in welding is the arc current. However, the penetration geometry depends not only on the total energy input to the metal but also on the energy flux distribution at the metal surface and the balance of whole forces in the welding phenomena [1-4], as shown in **Figure 1**.

This paper presents a methodology for predicting the geometry of the molten liquid produced by the arc. The whole region of gas tungsten arc welding consisting of a tungsten cathode, an arc plasma and a molten anode, namely, a weld pool is treated in a unified numerical model to take into account the close interaction between the arc plasma and the weld pool. The basic model and procedure are the same as our previous papers used [5, 6], but are extended to employ different shielding gases. We give predictions of the time dependent two-dimensional distributions of temperature and velocity in the whole region of gas tungsten arc welding process in argon and also in helium.

2. An Arc-Electrode Model

The tungsten cathode, arc plasma and anode are described relative to a cylindrical coordinate, assuming rotational symmetry around the arc axis. The calculation domain is shown in **Figure 2**. The flow is assumed to be laminar, and the arc plasma is assumed to be in the local thermodynamic equilibrium (LTE). Furthermore, the anode surface is assumed to be flat and unperturbed by the arc pressure. The diameter of the tungsten cathode is 3.2 mm with a 60 degrees conical tip. The anode is stainless steel SUS304 and its temperature coefficient of surface tension above the melting point is assumed as

† Received on November 7, 2005
* Designated researcher
** Associate professor
*** Professor emeritus

Transactions of JWRI is published by Joining and Welding Research Institute, Osaka University, Ibaraki, Osaka 567-0047, Japan

shown in **Figure 3** [7]. The governing equations, boundary conditions and numerical method have been detailed in our previous papers [5, 6], so that only the most pertinent points are explained here.
The mass continuity equation (1) is

$$\frac{\partial \rho}{\partial t}+\frac{1}{r}\frac{\partial}{\partial r}(r\rho v_r)+\frac{\partial}{\partial r}(\rho v_z)=0$$

the radial momentum conservation equation (2) is

$$\frac{\partial \rho v_r}{\partial t}+\frac{1}{r}\frac{\partial}{\partial r}(r\rho v_r^2)+\frac{\partial}{\partial z}(\rho v_z v_r)=-\frac{\partial P}{\partial r}-j_z B_\theta + \frac{1}{r}\frac{\partial}{\partial r}(2r\eta\frac{\partial v_r}{\partial r})+\frac{\partial}{\partial z}(\eta\frac{\partial v_r}{\partial z}+\eta\frac{\partial v_z}{\partial r})-2\eta\frac{v_r}{r^2}$$

the axial momentum conservation equation (3) is

$$\frac{\partial \rho v_z}{\partial t}+\frac{1}{r}\frac{\partial}{\partial r}(r\rho v_r v_z)+\frac{\partial}{\partial z}(\rho v_z^2)=-\frac{\partial P}{\partial z}+j_r B_\theta + \frac{\partial}{\partial z}(2\eta\frac{\partial v_z}{\partial z})+\frac{1}{r}\frac{\partial}{\partial r}(r\eta\frac{\partial v_r}{\partial z}+r\eta\frac{\partial v_z}{\partial r})+\rho g$$

the energy conservation equation (4) is

$$\frac{\partial \rho h}{\partial t}+\frac{1}{r}\frac{\partial}{\partial r}(r\rho v_r h)+\frac{\partial}{\partial z}(\rho v_z h)=\frac{1}{r}\frac{\partial}{\partial r}(\frac{r\kappa}{c_p}\frac{\partial h}{\partial r})+\frac{\partial}{\partial z}(\frac{\kappa}{c_p}\frac{\partial h}{\partial z}) + j_r E_r + j_z E_z - U$$

the current continuity equation (5) is

$$\frac{1}{r}\frac{\partial}{\partial r}(rj_r)+\frac{\partial}{\partial z}(j_z)=0$$

the Ohm's law (6) is

$$j_r=-\sigma\frac{\partial V}{\partial r};j_z=-\sigma\frac{\partial V}{\partial z}$$

and Maxwell's equation (7) is

$$\frac{1}{r}\frac{\partial}{\partial r}(rB_\theta)=\mu_0 j_z \quad .$$

Each physical symbol in the above equations indicates the same meaning as in general use.

At the anode surface, BE in Fig. 2, there are two sources of radial momentum as shown in Fig. 1. The first is the drag force, namely, the shear stress which is applied by the cathode jet on the surface of the weld pool, and the second is the surface tension gradient force, namely, the Marangoni force. The drag force is already reflected in equation (2) for the radial momentum conservation. The viscosity η makes the drag force at the anode surface. Therefore, the Marangoni force would need to be included in the radial momentum conservation at points on the anode surface, BE. In most cases, the difference in surface tension arises from the temperature variation at the weld pool surfaces [8], and then the Marangoni force τ can be expressed by

$$\tau=-\eta\frac{\partial v_r}{\partial z}=\frac{\partial \gamma}{\partial T}\frac{\partial T}{\partial r} \qquad (8)$$

where γ is the surface tension of the weld pool. Therefore, the additional term for equation (2) at the anode surface F_A is

Anode $$F_A=\frac{\partial}{\partial z}\left(\frac{\partial \gamma}{\partial T}\frac{\partial T}{\partial r}\right) \quad . \qquad (9)$$

The differential equations (1) to (7) are solved iteratively by the SIMPLEC numerical procedure [9] for the whole region of the stationary gas tungsten arc welding process as shown in Fig. 2.

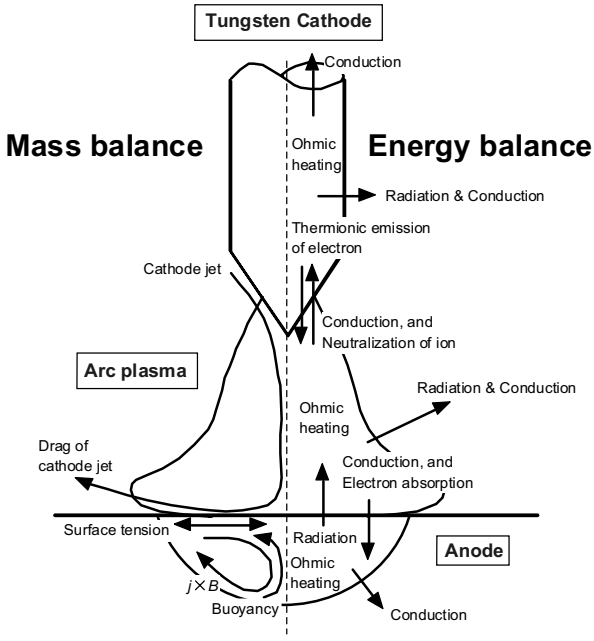

Fig. 1 Schematic illustration of energy and mass balance in the arc melting/welding process.

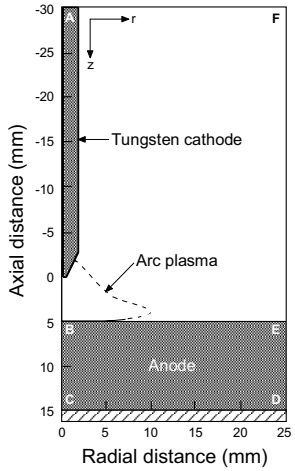

Fig. 2 Schematic illustration of calculated domain.

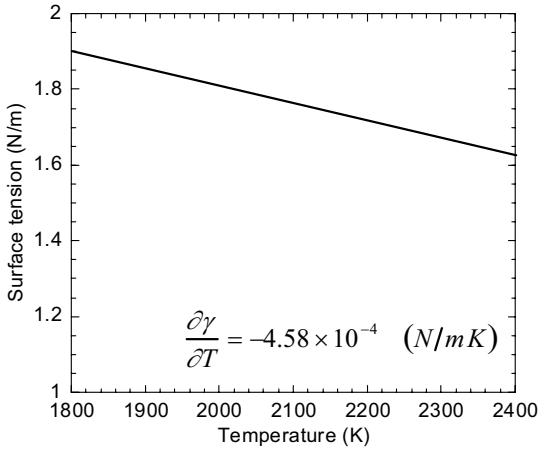

Fig. 3 Assumption of surface tension of molten SUS304 [7].

3. Results and Discussion

3.1 Argon shielding gas

Figure 4 shows distributions of temperature and fluid flow velocity of the weld for the individual driving forces in argon gas tungsten arc. These calculations were made in the steady state under the conditions of a welding current 150 A and an arc gap 5 mm. Each calculation was carried out by taking into account the driving force for the drag of the cathode jet in equation (2), the buoyancy in equation (3), the electromagnetic in equations (2) and (3), and the Marangoni in equation (9). Each maximum velocity for drag of cathode jet, buoyancy, electromagnetic and Marangoni force is 47 cm s^{-1}, 1.4 cm s^{-1}, 4.9 cm s^{-1} and 18 cm s^{-1}, respectively. Fig. 4 suggests that the calculated convective flow in the weld pool is dominated by the drag force of the cathode jet and the Marangoni force as compared with the other two driving forces in argon arc.

Figure 5 represents the two-dimensional distributions of temperature and of fluid flow velocity in the whole region of the stationary gas tungsten arc weld for a 150 A welding current at 20 seconds after arc ignition. The maximum calculated velocity of the cathode jet in Fig. 5 reaches 201 m s^{-1}. This cathode jet changes its direction in front of the anode surface, and then its radial component of fluid flow drags the surface of the weld pool. The outward fluid flow is also caused by a normal negative temperature coefficient of surface tension as shown in Fig. 3. Fig. 5 represents a numerical result corresponding to strong outward fluid flow with a wide and shallow weld penetration which is caused by both outward forces of the drag force and the Marangoni force. This weld penetration geometry is a typical one in the argon gas tungsten arc welding process. The maximum calculated velocity in the weld pool for all considered cases reaches 54 cm s^{-1} at 20s after arc ignition.

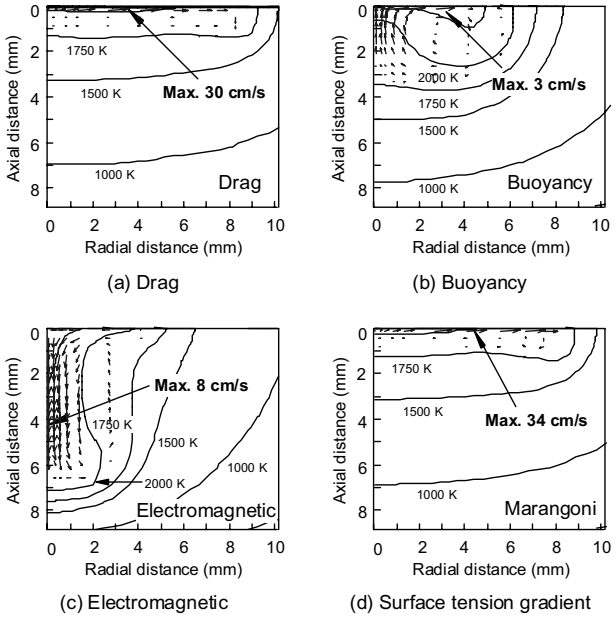

Fig. 4 Temperatures and fluid flow velocities in the welds for individual driving forces in argon arc.

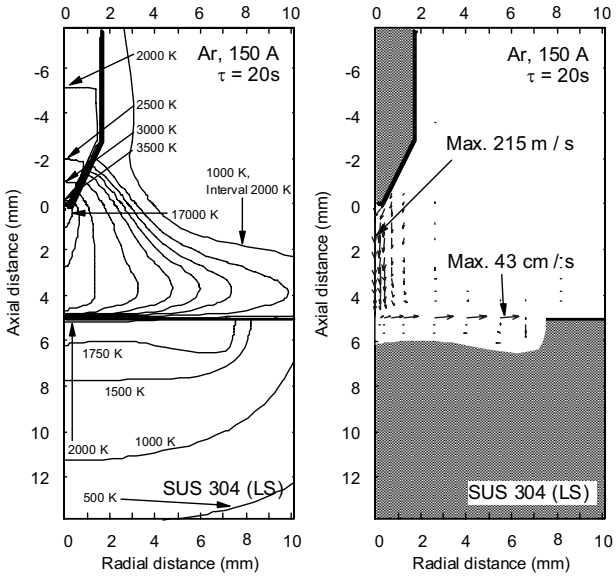

Fig. 5 Two-dimensional distributions of temperature and of fluid flow velocity at 20 seconds after arc ignition for a 150 A in argon gas tungsten arc weld on SUS304.

3.2 Argon shielding gas

Figure 6 shows the radius distributions of current density at the surface of a water cooled copper anode for 150 A of arc current, in the cases of argon and helium. These calculations were made in the steady state. The current density in the helium arc is much more intense than that in the argon arc, which suggests that the electromagnetic force in the weld pool becomes a major force in the helium gas tungsten arc. The electrical conductivity for helium plasma is significantly smaller than that of argon plasma for T < 10,000 K due to the

higher ionization potential of He [10]. For example, the electrical conductivity at 8,000 K is about only 1 A/Vm for helium plasma but about 1,000 A/Vm for argon plasma [10]. It can be deduced from this low electrical conductivity that constriction of the helium arc close to the anode surface occurs.

Figure 7 shows the same distributions as in Fig. 4 for the individual driving forces but for the helium gas tungsten arc. Each maximum velocity for drag, buoyancy, electromagnetic and Marangoni force is 11 cm s^{-1}, 8 cm s^{-1}, 25 cm s^{-1} and 66 cm s^{-1}, respectively. Fig. 7 suggests that the calculated convective flow in the weld pool is dominated by the electromagnetic force and the Marangoni force in the helium arc.

Figures 8 represent the two-dimensional distributions of temperature and of fluid flow velocity in the whole region of the helium gas tungsten arc welding for 150 A of welding current, 20 seconds after arc ignition. The weld penetration increases with the elapse of time. It is found, in Fig. 8, that there are two re-circulatory flows in the weld pool, namely, an inward fluid flow close to the center at the inner of the weld pool and an outward fluid flow at the surface of the weld pool. The inward fluid flows is caused by the electromagnetic force. The outward fluid flow is principally caused by the Marangoni force with a normal negative temperature coefficient of surface tension. Both driving forces dominate the re-circulatory flows in the weld pool, and then a special geometry of weld penetration appears as shown in Fig. 8, which is obviously changed in comparison with that in argon arc.

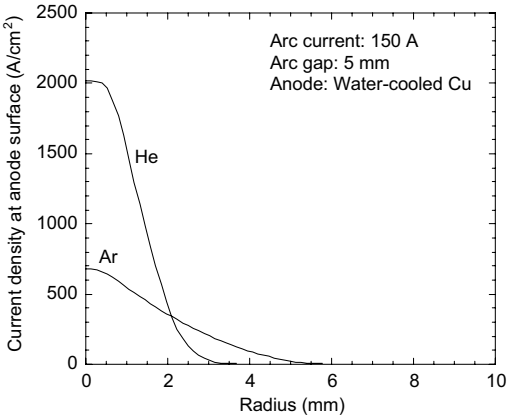

Fig. 6 Radius distributions of current density at the surface of a water cooled copper anode for argon arc and helium arc for a 150 A in arc current.

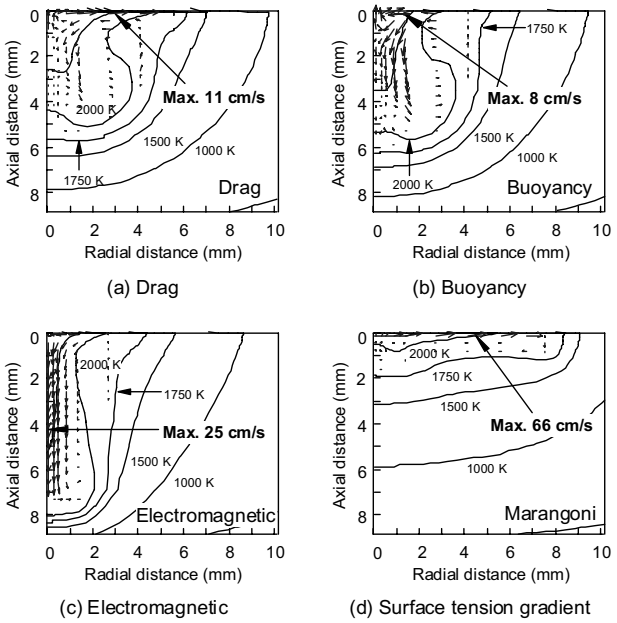

Fig. 7 Temperatures and fluid flow velocities in the welds for individual driving forces in helium arc.

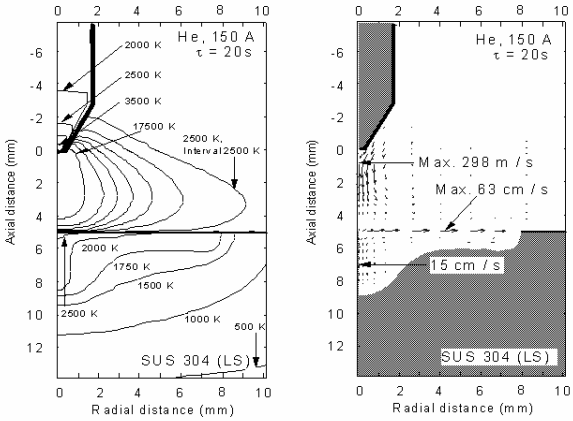

Fig. 8 Two-dimensional distributions of temperature and of fluid flow velocity at 20 seconds after arc ignition for a 150 A in a helium gas tungsten arc welding of SUS304.

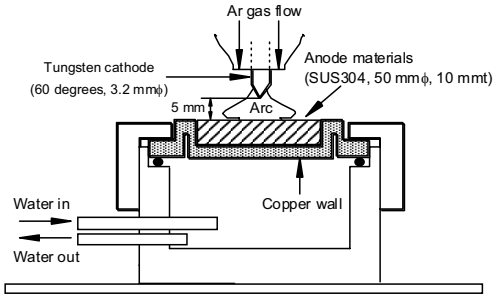

Fig. 9 Schematic illustration of the apparatus for stationary gas tungsten arc weld on SUS304.

3.3 Predictions with experimental results

Stationary gas tungsten arc welding was performed for comparison of the weld penetrative profiles with calculated results for argon arc and helium arc. The experimental setup is shown in **Figure 9**. The anodes were disks, 50 mm in diameter and 10 mm in thickness, of SUS304, mounted into a water-cooled copper plate. The experiments were made for 20s of arcing time allow comparison of experiment with theory, so that conditions were then similar to the boundary condition of calculations, to be comparable to the results of calculations.

Figures 10 and **11** show predicted weld penetrative profiles after 20 seconds, compared with experimental results, in the case of argon and helium, respectively. We consider that the agreement between the theoretical predictions and the experimental weld profiles of Figs. 10 and 11 is very good. The deep penetration at the center of the weld, which would be caused by the electromagnetic force, in the helium arc was experimentally observed and was similar to the theoretical prediction, whereas its deep penetration at the center was not found in prediction of experiment in the argon arc.

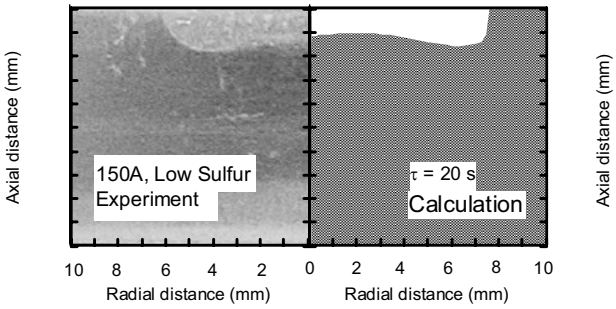

Fig. 10 Comparison of experimental and theoretical weld profiles from 150 A after 20s in an argon arc.

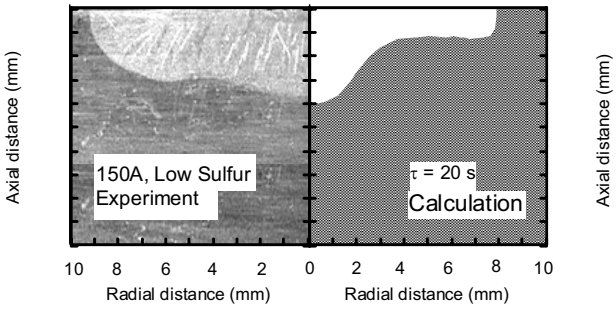

Fig. 11 Comparison of experimental and theoretical weld profiles from 150 A after 20s in helium arc.

4 Conclusions

The conclusions in the present paper are summarized as follows.

(1) The whole region of the stationary gas tungsten arc welding process, namely, tungsten cathode, arc plasma and anode was treated in a unified numerical model to take into account the close interaction between the arc plasma and the liquid anode.
(2) Calculations were made for the time dependent development of the penetration of the anode for the arc plasma in different gaseous atmosphere, namely, in argon and also in helium.
(3) The calculated maximum velocities of the weld pool for each force, namely, drag of cathode jet, buoyancy, electromagnetic and Marangoni force were 47, 1.4, 4.9 and 18 cm s^{-1}, respectively, in argon gas tungsten arc welding.
(4) The calculated maximum velocities of the weld pool for each force, namely, drag of cathode jet, buoyancy, electromagnetic and Marangoni force were 11, 8, 25 and 66 cm s^{-1}, respectively, in helium gas tungsten arc welding.
(5) The above numerical calculations showed that the calculated convective flow in the weld pool was principally dominated by the Marangoni force independently of the gaseous atmosphere. However, another dominant force was the drag force of the cathode jet in the argon arc and the electromagnetic force in the helium arc.
(6) It was concluded that a balance of these driving forces could change the direction of re-circulatory flow in the molten anode and dramatically varied the weld penetration geometry.

References

[1] Oreper G.M., et al.; *Welding J.*, 1983; 62: p307s-312s.
[2] Choo R.T.C., et al.; *Welding J.*, 1992; 71: p77s-93s.
[3] Matsunawa A.; *Proc. 3rd Int. Conf. Trends in Welding Res.*, Gatlinburg, Tennessee, USA, 1992; 3: p3-16.
[4] Goodarzi M., et al.; *J. Phys. D: Appl. Phys.*, 1998; 31: p569-583.
[5] Tanaka M., et al.; *Metall. Trans. A*, 2002; 33A: p2043-2052.
[6] Tanaka M., et al.; *Plasma Chem. & Plasma Process.*, 2003; 23: p585-606.
[7] Zacharia T., et al.; *Metall. Trans. B*, 1990; 21B: p600-603.
[8] David S.A., et al.; *MRS Bulletin*, 1994; 19 (1): p29-35.
[9] Patanker S.V.; *Numerical Heat Transfer and Fluid Flow*, Hemisphere Publishing Corporation, 1980.
[10] Boulos M.I., et al.,; *Thermal Plasmas*, Plenum Press, 1994.